

Alcator C-Mod predictive modeling

Alexei Pankin, Glenn Bateman, and Arnold Kritz
Lehigh University, 16 Memorial Drive East, Bethlehem, Pennsylvania 18015

Martin Greenwald, Joseph Snipes, and Thomas Fredian
Massachusetts Institute of Technology, 175 Albany Street, Cambridge, Massachusetts 02139

(Received 3 April 2001; accepted 9 July 2001)

Predictive simulations for the Alcator C-mod tokamak [I. Hutchinson *et al.*, *Phys. Plasmas* **1**, 1511 (1994)] are carried out using the BALDUR integrated modeling code [C. E. Singer *et al.*, *Comput. Phys. Commun.* **49**, 275 (1988)]. The results are obtained for temperature and density profiles using the Multi-Mode transport model [G. Bateman *et al.*, *Phys. Plasmas* **5**, 1793 (1998)] as well as the mixed-Bohm/gyro-Bohm transport model [M. Erba *et al.*, *Plasma Phys. Controlled Fusion* **39**, 261 (1997)]. The simulated discharges are characterized by very high plasma density in both low and high modes of confinement. The predicted profiles for each of the transport models match the experimental data about equally well in spite of the fact that the two models have different dimensionless scalings. Average relative rms deviations are less than 8% for the electron density profiles and 16% for the electron and ion temperature profiles. © 2001 American Institute of Physics. [DOI: 10.1063/1.1399057]

I. INTRODUCTION

Integrated predictive transport codes are widely used to validate theoretical transport models and to plan experiments. At the present time, predictive transport models are able to reproduce fundamental features of tokamak transport such as confinement time scaling, as well as predicting the profiles of temperature, density, and current. A comparison of the 12 most widely used transport models^{1,2} suggests that the Multi-Mode model (MMM95)³⁻⁵ and the mixed-Bohm/gyro-Bohm (JET)⁶⁻⁸ model are among the best models used in integrated transport modeling codes to reproduce the experimentally measured temperature and density profiles and energy content for both low-mode (L-mode) and high-mode (H-mode) discharges. Both models are available in the BALDUR predictive transport code.⁹

The BALDUR time-dependent $1\frac{1}{2}$ transport code, which has been developed over the last three decades at the Princeton Plasma Physics Laboratory (PPPL) and Lehigh University, computes the time evolution of plasma profiles given time-dependent boundary conditions. These conditions are taken from experimental data whenever possible. The BALDUR code computes heat and particle sources (such as neutral beam injection heating), sinks (such as impurity radiation), transport fluxes, fusion reactions, magneto-hydrodynamic equilibrium, and the effect of large-scale instabilities (such as sawtooth oscillations). Recycling and gas puffing are represented by the influx of hydrogenic and impurity neutrals, which have the effect of controlling the time evolution of the average plasma density and impurity fraction. The BALDUR code supports a number of different theoretical and empirical transport models. The simulations in this paper use two models—the Multi-Mode model and the mixed-Bohm/gyro-Bohm model. Neoclassical transport is included independently with both models.

The Multi-Mode model includes contributions to trans-

port from drift modes¹⁰ and pressure-driven modes.¹¹ Simulations of more than 40 discharges from TFTR (Tokamak Fusion Test Reactor),¹² DIII-D (Doublet III-D),¹³ and JET (Joint European Torus)¹⁴ have been carried out using the Multi-Mode model, and the resulting temperature and density profiles have been compared with experimental data. These comparisons have produced agreement within the range of 15% rms for temperature and density profiles and 9% rms for plasma energy content.⁵

The mixed-Bohm/gyro-Bohm model is an empirically based anomalous transport model. The model consists of a Bohm term, developed to fit JET data and to represent transport due to long-wavelength turbulence, and a gyro-Bohm term, required to fit discharges in smaller tokamaks and to represent small-scale drift-wave turbulence. The results from the Multi-Mode and mixed-Bohm/gyro-Bohm models are compared in Refs. 15, 16. On average, simulations using these two models were found to agree with experimental data equally well.

Tokamak devices differ in geometry, operational scenarios, and confinement modes. Alcator C-Mod¹⁷ differs in several ways from the other tokamaks simulated with the BALDUR code previously. Alcator C-Mod is a compact high-field divertor tokamak. The average plasma density is typically in the range of $(1 \text{ to } 5) \times 10^{20} \text{ m}^{-3}$. Moreover, densities above 10^{21} m^{-3} have been achieved. Alcator C-Mod provides operational regimes free of large type I edge localized modes (ELM) for the duration of the H-mode.^{18,19} All of this makes Alcator C-Mod a good tokamak for experimental testing of the ideas used in the design of the medium-size high-field tokamak reactors such as FIRE²⁰ or IGNITOR.^{21,22} The task of the current paper is to compare simulation results obtained with the Multi-Mode model and the mixed-Bohm/gyro-Bohm model for seven L-mode and H-mode Alcator C-Mod discharges.

This paper is organized as follows: In Sec. II, we introduce BALDUR predictive transport code and describe the Multi-Mode model and the mixed-Bohm/gyro-Bohm model. A brief description of Alcator C-mod and the discharges used in the simulations is presented in the Sec. III. In Sec. IV, results of the numerical simulations are shown. Electron and ion temperature profiles and electron density profile are compared with experimental data and with processed data obtained from EFIT and TRANSP analysis. The numerical results from both transport models are found to be in reasonable agreement with the experimental data. Section V contains a statistical comparison of the simulation results and the experimental data. Conclusions are presented in the Sec. VI.

II. BALDUR PREDICTIVE TRANSPORT CODE

BALDUR is a $1\frac{1}{2}$ -dimensional integrated predictive transport code designed to simulate a wide variety of plasma conditions in tokamaks.⁹ The BALDUR code describes, as a function of magnetic flux surface, the time evolution of electron and ion temperatures, charged particle densities (up to two hydrogenic species and up to four impurity species), and the poloidal magnetic flux density. The shapes of the flux surfaces are determined by solving axisymmetric equilibrium force balance equations, given time-dependent boundary conditions. We use the equilibrium moments code VMCE2^{23,24} within the BALDUR code.

The transport models embedded in the BALDUR predictive code are primarily theory based and have gyro-Bohm scaling. An exception is the empirical mixed-Bohm/gyro-Bohm model (JET), which principally has Bohm scaling. The Multi-Mode model and the mixed-Bohm/gyro-Bohm model have very different scaling with the respect to plasma parameters and different dependence on the shape of plasma profiles.

The sources and sinks in the BALDUR transport code are computed with a variety of algorithms, which include neutral beam injection (NBI), fusion, radiative losses, ohmic heating, neutral impurity influxes. Alcator C-Mod has radio frequency heating in the range of the ion cyclotron resonance frequencies (ICRF). The heating of the electrons and ions is input in the BALDUR code as a function of time and radius.

The BALDUR code has various options available to treat the axisymmetric effects of large-scale instabilities such as sawtooth oscillations, saturated tearing modes, and high- n ballooning modes. The BALDUR code uses a sawtooth model, based on Kadomtsev mixing.²⁵ Sawtooth crash times are specified as inputs, in order to synchronize with experimental data, and the mixing of the current and fast particles (beam products and fusion products) is computed in the BALDUR code.

A. Multi-Mode model

We used the 1995 version of the Multi-Mode model. This version of the model has been tested for more than 40 discharges in TFTR, DIII-D, and JET and is described in detail in Refs. 5 and 26. The core of the Multi-Mode is the Weiland transport quasi-linear fluid model for the ion-temperature-gradient (ITG) and the collisionless trapped

electron (CTE) modes. This model takes into account inhomogeneities of temperature, density, and magnetic field in the radial direction, electromagnetic effects, effects of finite-Larmor radius, trapped electrons, impurities, fast ions, and finite β . Radial electron and ion heat fluxes and hydrogenic and impurity charged particle fluxes are derived from fluid equations for each plasma species. Effective diffusion coefficients computed in this quasi-linear model are logically equivalent to the form:²⁷

$$\chi_j \propto \frac{\gamma^3/k_x^2}{(\omega_r - \frac{5}{3}\omega_{Dj})^2 + \gamma^2}, \quad (1)$$

where index j represents ion, electrons, and impurities, k_x is the inverse radial correlation length, $(\omega_r + i\gamma)$ is the eigenvalue for each of the modes contributing to the transport, and ω_{Dj} is the diamagnetic drift frequency. The effective diffusivities have a gyro-Bohm scaling, which results from fixing the space scale of the turbulence equal to the scale of the most unstable mode $(\rho_s k_\theta)^2 = 0.1$. Despite the intrinsic B_T^{-1} gyro-Bohm scaling, previous simulation results suggested that total observed transport scaling may be an artifact of the way in which the sources, sinks, and plasma profiles change as the number of gyro-radii across the plasma change.^{4,15,16} Close to the axis ($r/a \leq 0.3$), the anomalous drift transport coefficients become negligible and neoclassical transport (see Sec. III C) and transport due to kinetic-ballooning modes dominate. The 1995 Multi-Mode model includes the Guzdar–Drake model¹¹ for transport associated with drift-resistive ballooning modes and a kinetic-ballooning model for transport associated with these modes.

B. The mixed-Bohm/gyro-Bohm model

The mixed-Bohm/gyro-Bohm (JET) model was originally developed to fit experimental data from the JET tokamak, which commonly exhibit Bohm scaling.^{6–8,28} The JET model is a nonlocal model, which describes the effect of large-scale perturbations at the plasma edge, such as edge localized modes (ELMs). In order to match experimental data in smaller tokamaks, a gyro-Bohm term was added. The Bohm term remains dominant, except in the deep core of the plasma and except in the case of smaller tokamaks with low magnetic field. Transport diffusivities in the model are also functions of the profile shapes (characterized by normalized gradients) and other plasma parameters such as magnetic q .

The ion and electron thermal diffusion coefficients in the JET model are the combination of the Bohm and gyro-Bohm terms with empirically determined coefficients:

$$\chi_{i,e}^{\text{JET}} = \rho_* c_s \left(C_{e,i}^B q^2 \frac{a}{p_e} \frac{dp_e}{dr} \Delta_{T_e} + C_{e,i}^{gB} \rho_* \frac{a}{T_e} \frac{dT_e}{dr} \right), \quad (2)$$

where $C_i^B = 2C_e^B = 1.6 \times 10^{-4}$ and $C_e^{gB} = 2C_i^{gB} = 3.5 \times 10^{-2}$ are empirical coefficients, and

$$\Delta_{T_e} \equiv \frac{T_e|_{r/a=0.8}}{T_e|_{r/a=1.0}} - 1 \quad (3)$$

is a finite difference approximation to the normalized temperature electron temperature difference at the plasma edge.

TABLE I. Notation used in this paper.

| | | |
|----------------------------|----------|--|
| a | m | plasma minor radius (half-width) |
| r | m | flux surface minor radius (half-width) |
| R | m | major radius to geometric center of each flux surface |
| κ | | plasma elongation |
| δ | | plasma triangularity |
| B_T | T | vacuum toroidal magnetic field at center of flux surface |
| I_p | A | toroidal plasma current |
| n_e | m^{-3} | electron density |
| Z_{eff} | | measure of the impurity concentration |
| P_{aux} | MW | auxiliary heating power |
| T_e | keV | electron temperature |
| T_i | keV | ion temperature |
| m_i | kg | average ion mass |
| c_s | m/s | sound speed $[(k_b T_e / m_i)^{1/2}]$ |
| ω_{ci} | 1/s | ion gyro-frequency $[e B_T / m_i]$ |
| ω_{De}, ω_{Di} | 1/s | magnetic drift frequencies |
| ρ_s | m | gyro-radius $[c_s / \omega_{ci}]$ |
| ρ_* | | normalized gyro-radius $[\rho_s / a]$ |
| β | | beta $[k_b (n_e T_e + n_i T_i) / (B_T^2 / 2 \mu_0)]$ |
| ν_{*e} | | collisionality $[\nu_{ei} q R^{5/2} / (v_e r^{3/2})]$ |
| ν_{ei} | 1/s | electron-ion collision frequency |
| v_e | m/se | electron thermal velocity $[(k_b T_e / m_e)^{1/2}]$ |
| q | | magnetic q -value |

Other variables in Eq. (2) are described in Table I. The first term in Eq. (2) represents Bohm contribution and the second represents gyro-Bohm contribution.

The charged particle diffusion coefficient is given by

$$D^{B/gB} \equiv \left(1 - 0.7 \frac{r}{a} \right) \frac{\chi_i \chi_e}{\chi_i + \chi_e}. \quad (4)$$

C. Neoclassical transport

Neoclassical thermal and particle contributions are added to each of the anomalous transport models described above. The Hawryluk–Hirshman model²⁹ for neoclassical particle transport and the Chang–Hinton model³⁰ for neoclassical thermal transport are used in the BALDUR code.

III. ALCATOR C-MOD

Alcator C-Mod is high-field ($2.6 < B_T < 7.9$ T), relatively small tokamak (major radius $R = 0.67$ m, minor radius $a = 0.22$ m)¹⁷ with a single-null-bottom divertor and ion cyclotron range of frequencies (ICRF) heating. In this paper, a series of seven discharges are simulated. These discharges have plasma currents ranging from 0.80 to 1.02 MA, toroidal fields, from 5.21 to 5.42 T, and average electron densities, from 0.925 to $3.86 \times 10^{20} \text{ m}^{-3}$. The elongation varied from 1.59 to 1.65, and average triangularity was about 0.42. The actual normalized gyro-radii $\rho_* = \sqrt{2 T_e M_i} / (e B a)$, computed using the experimentally measured electron temperature, are in the range from 8.5×10^{-3} to 11.0×10^{-3} , which is in the upper range of normalized gyro-radii previously simulated with the BALDUR code for other tokamaks.^{4,15,16}

A. Operational regimes

Both L-mode and H-mode discharges were intensively studied on Alcator C-Mod.^{18,31} The four L-mode discharges

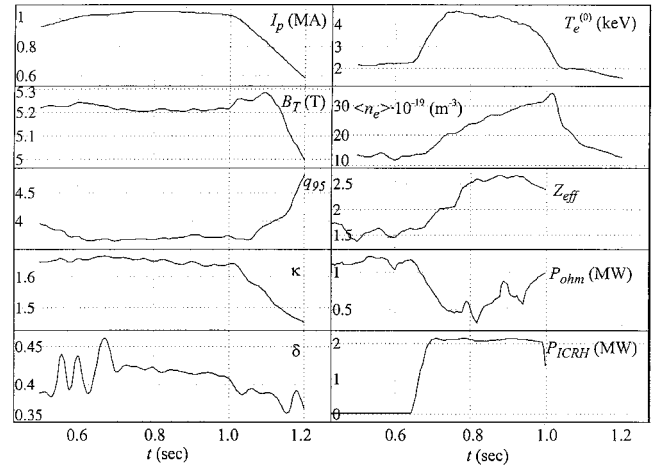


FIG. 1. Experimental scenario for Alcator C-Mod 960116024. Panels show the time evolution of plasma current I_p , toroidal magnetic field B_T , q_{95} , elongation κ , triangularity δ , central electron temperature $T_e^{(0)}$, volume average density $\langle n_e \rangle$, Z_{eff} , Ohmic heating power, and ICRH heating power.

and three H-mode discharges were selected for the simulations with the BALDUR code. The three H-mode discharges and three of the L-mode discharges analyzed in this paper occur when the ion ∇B drift is directed toward a single null X point.³² The fourth L-mode discharge has the ion ∇B drift in the opposite direction.

High-power rf heated ($P_{\text{rf}} \geq 2$ MW) Alcator C-Mod discharges make the transition into H-mode discharges over wide range of conditions.^{32,33} H-mode was observed to occur in all operating ranges of magnetic field B_T , plasma current I_p and, in some discharges, with a line average density \bar{n} as high as $4.8 \times 10^{20} \text{ m}^{-3}$. H-modes are either Ohmic or heated by ICRF heating. Radio-frequency absorption efficiency on Alcator C-Mod is typically greater than 80%.³⁴ Many H-mode discharges do not indicate the presence of large and regular type I ELMs.^{18,19,35} In Alcator C-Mod, an enhanced D_α (EDA) H-mode¹⁹ occurs with lower particle and impurity confinement. This D_α mode resembles H-modes with ELMs on other machines. Nevertheless the D_α mode still has good energy confinement and provides a promising operational regime. Alcator C-Mod shows also some special enhanced confinement modes, such as the pellet enhanced performance (PEP) mode³⁶ and recently discovered the ITB/PEP mode associated with spontaneous formation of short-lived internal transport barriers in the core of the plasma.³⁷

An example of an ICRH heated H-mode scenario is shown in Fig. 1. The results of the TRANSP analysis, which are shown in Fig. 1, are smoothed in time over the sawtooth oscillations. Sawteeth are present in Alcator C-Mod discharges with very few exceptions.³⁸ The sawtooth period varies from 3 to 8 ms in the Ohmic stage, from 4 to 18 ms in ICRF heated L-modes, and from 6 to 25 ms in ICRF heated H-modes. The period increases monotonically with stored energy. At the same time, the amplitude of sawtooth crashes also increase with stored energy, running up to the half of the peak temperature value.

B. Experimental diagnostics

Electron density and temperature profiles are accurately measured in Alcator C-Mod. The electron density profile is measured using an interferometer with ten vertical chords. In addition, reflectometry is also used on Alcator C-Mod for electron density measurements.³⁹ Five amplitude-modulated channels at 50, 60, 75, 88, and 110 GHz are used to produce a differential signal and to reconstruct density profiles from the measured group delays. The channel at 88 GHz also measures the signal of each sideband for density fluctuations studies. The time resolution is $2.4 \mu\text{s}$ for the density fluctuations and 0.5 ms for the profile measurements. Electron temperature profiles are measured by electron cyclotron emission (ECE) grating polychromator and a Thomson scattering system. Nine channels of the ECE provide time-dependent electron temperatures at nine radii. The absolute calibration uncertainties are estimated as $\pm 10\%$.⁴⁰ The ECE grating polychromator is also used for ICRF power deposition measurements.⁴¹ The Thomson scattering (TS) system has six spatial channels with observation volumes between the midplane and the edge of the plasma.⁴² The electron temperature is measured by the TS system in the range 200 eV to 10 keV with a time resolution of 20 ms. The radiated power is measured by the bolometric diagnostic system, which is based on an array of 16 foil bolometers and silicon AXUV photodiodes. The AXUV system consists on a single channel AXUV detector, two 16 channels central arrays, and one 20 channels edge array located inside the rf protection limiter. The bolometric system provides spatial resolution of 2 mm for the edge array and a time resolution at least $100 \mu\text{s}$.^{40,43} The ICRF power deposition is calculated using the FPPRF Fokker–Plank code combined with either the SPRUCE⁴⁴ or TORIC⁴⁵ code.

All experimental data are represented on the surfaces of the normalized poloidal flux ψ . The equilibrium is reconstructed on the base of magnetic diagnostics with the EFIT code.⁴⁶ The accuracy in determining of the location of the last closed flux surface is about $\pm 3 \text{ mm}$.⁴⁰ The EFIT code is also used to estimate the stored energy. The stored energy in the energetic minority ions is calculate with TRANSP⁴⁷ and the toroidal full-wave code SPRUCE.⁴⁸

IV. SIMULATION RESULTS

In this section, the results of the simulations obtained using the Multi-Mode or mixed-Bohm/gyro-Bohm transport models in the BALDUR predictive transport code are presented. The temperature and density profiles were initialized during the Ohmic stage of each discharge and the profiles evolved in each simulation through the auxiliary heated stage. The simulations are performed in the region $0 \leq r/a \leq 0.9$ with the boundary conditions taken from the experimental data and with zero derivatives imposed on the axis for each profile. Boundary values of hydrogenic and impurity densities were estimated from the experimental values of Z_{eff} and the electron density. An impurity with effective charge state of 10 was used in the simulations. Hydrogenic gas puffing was used in the simulations to control the average plasma density as a function of time. Time-dependent profiles of rf

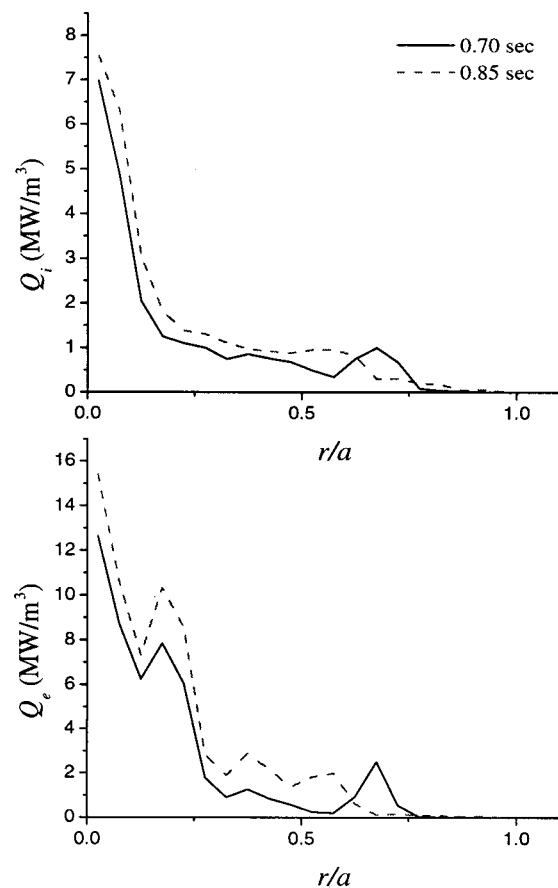


FIG. 2. Power deposition profiles for Alcator C-Mod 960301009 at 0.7 s and 0.85 s.

power deposition, reconstructed from the MDSplus database, were used for rf heated discharges. Experimental data suggest that 55%–75% of the injected power is released to the thermal electrons and the deposition profile is usually peaked at the center (see Fig. 2).

Seven Alcator C-Mod discharges were selected for the simulations. Three of these discharges are normal L-mode discharges (950407013, 960126007, and 960229042). One discharge is an enhanced L-mode discharge (960301009) with a reversed toroidal field and current, in which ion $B \times \nabla B$ drift is directed away from the active lower divertor. One discharge (960116024) is an ELM-free H-mode discharge. Two discharges (960116027 and 960214017) are enhanced D_α (EDA) discharges. These discharges cover most of the standard operational regimes of Alcator C-Mod (see Sec. III A). The L-mode discharge parameters are tabulated in Table II and the H-mode discharges in Table III. To illustrate the agreement between simulation profile results and measurements, plots are included in this paper for three of four L-mode discharges and two of the three H-mode discharges. In the statistical analysis of the comparison, in Sec. V, all seven C-Mod discharges are included.

A. Simulation of the L-mode discharges

Table II lists the main parameters of the discharges simulated in this section. The density and temperature profiles are compared with the experimental data as a function of minor

TABLE II. Major plasma parameters for L-mode discharges.

| C-mod discharge | 950407013 | 960126007 | 960229042 | 960301009 |
|--|-----------|-----------|-----------|-----------|
| R (m) | 0.673 | 0.673 | 0.673 | 0.672 |
| a (m) | 0.210 | 0.217 | 0.219 | 0.218 |
| κ_a | 1.64 | 1.65 | 1.64 | 1.61 |
| δ | 0.42 | 0.41 | 0.42 | 0.44 |
| B_T (T) | 5.38 | 5.24 | 5.38 | 5.42 |
| I_p (MA) | 1.01 | 0.80 | 1.00 | 0.83 |
| $\bar{n}_e \times 10^{-20}$ (m^{-3}) | 1.52 | 0.93 | 1.82 | 1.50 |
| \bar{Z}_{eff} | 2.02 | 2.38 | 2.02 | 1.85 |
| $\rho_*(0)$ | 0.0094 | 0.0085 | 0.010 | 0.011 |
| P_{aux} (MW) | 2.7 | 1.4 | 2.2 | 2.8 |
| Diagnostic time (s) | 0.83 | 0.99 | 0.99 | 0.99 |

radius in Figs. 3, 4, and 5 for three L-mode discharges, 950407013, 960229042, and 960301009. These plots show the results of simulations using the Multi-Mode model as well as results using the mixed-Bohm/gyro-Bohm models. The simulations using the two different transport models agree equally well with the experimental data for both density and temperature profiles. A statistical comparison is described in Sec. V.

The Multi-Mode model calculates effective ion and electron thermal diffusivities defined as the total ion or electron heat flux divided by the relevant density and the temperature gradient. The effective thermal diffusivities as a function of minor radius are shown in Fig. 6(a) for Alcator C-Mod discharge 960229042. The main contributions to the thermal diffusivities in these MMM95 simulations are produced by drift ITG/CTE modes, resistive ballooning modes, and neoclassical transport. Neoclassical transport dominates near the magnetic axis in the region $r/a < 0.2$, whereas ITG/CTE modes provide the main contribution in the region $0.2 \leq r/a < 0.8$. The dominant contributor to the ion thermal diffusivity χ_i in the outer region of the plasma is the resistive ballooning mode. For the electron thermal diffusivity χ_e , while ITG/CTE and the resistive ballooning modes still dominate in the region $r/a > 0.2$, the kinetic ballooning mode competes with the neoclassical transport in the center and dominates when $0.1 < r/a \leq 0.2$.

The diffusivities calculated in mixed-Bohm/gyro-Bohm model are shown in Fig. 6(b) for discharge 960229042. It can be seen that the contribution from the neoclassical transport

TABLE III. Major plasma parameters for H-mode discharges.

| C-mod discharge | 960116024 | 960116027 | 960214017 |
|--|-----------|-----------|-----------|
| Confinement regime | ELM free | EDA | EDA |
| R (m) | 0.676 | 0.676 | 0.677 |
| a (m) | 0.221 | 0.219 | 0.222 |
| κ_a | 1.65 | 1.65 | 1.59 |
| δ | 0.41 | 0.42 | 0.41 |
| B_T (T) | 5.22 | 5.22 | 5.21 |
| I_p (MA) | 1.01 | 1.02 | 1.02 |
| $\bar{n}_e \times 10^{-20}$ (m^{-3}) | 3.17 | 3.86 | 3.36 |
| \bar{Z}_{eff} | 2.40 | 1.41 | 1.49 |
| $\rho_*(0)$ | 0.0099 | 0.0096 | 0.0092 |
| P_{aux} (MW) | 2.35 | 2.7 | 2.5 |
| Diagnostic time (s) | 0.99 | 0.99 | 0.99 |

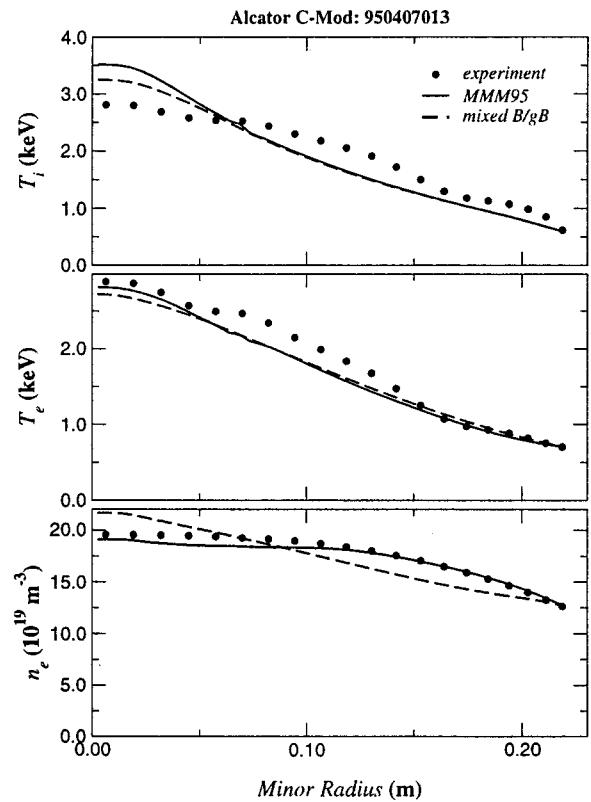


FIG. 3. Comparison of the experimental profiles ion and electron temperatures and electron density profiles with profiles predicted using the Multi-Mode model 95 and the mixed-Bohm/gyro-Bohm model for Alcator C-Mod 950407013.

dominates over the the inner one-third of the plasma for the ion diffusivity χ_i . The Bohm term gives the second largest contribution in the deep core and it exceeds the contribution from neoclassical transport in the outer region of the plasma, when $r/a \geq 0.3$. For the electron thermal diffusivity χ_e , the gyro-Bohm term competes with the Bohm contribution to the transport, when $r/a < 0.3$. The neoclassical contribution to transport is dominant near the magnetic axis, and the Bohm contribution is dominant in the outer region of the plasma.

The Multi-Mode and the mixed-Bohm/gyro-Bohm models have different scaling, particularly gyro-radius scaling, but BALDUR simulations using these two transport models match experimental data equally well. The Multi-Mode model is very sensitive to the changes of the shape of profile. Small deviations from self-similarity have a large effect on the resulting transport because of the sensitivity of the drift wave stability close to the marginal stability. For example, in L-mode discharges, it has been shown that the changes in the penetration depth of the edge neutrals cause changes of the edge collisionality and normalized gradient and affect the ITG mode.^{4,27} The characteristic gyro-Bohm scaling can be masked and the observed transport does not follow the intrinsic scaling. As a result, the Multi-Mode model works well for discharges with different transport scalings.

B. Simulation of the H-mode discharges

The parameters for the three H-mode discharges, for which the simulations are carried out, are listed in the Table

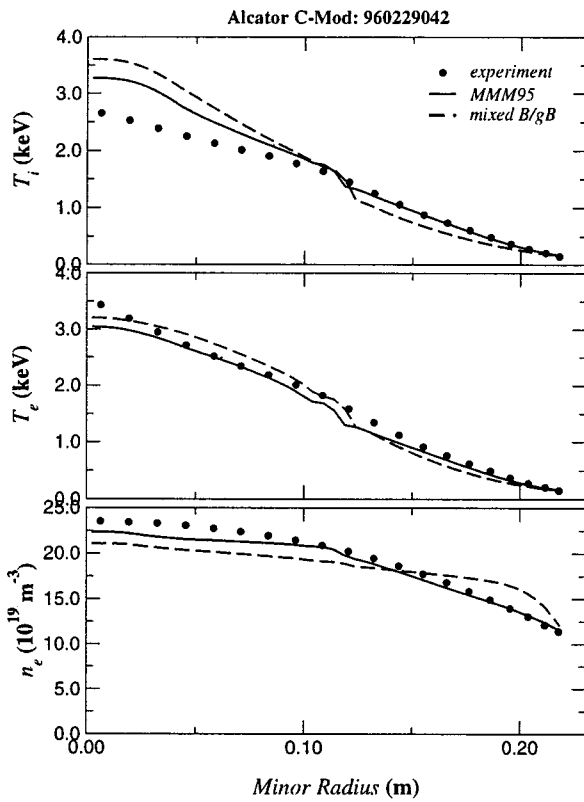


FIG. 4. Comparison of the experimental profiles ion and electron temperatures and electron density profiles with profiles predicted using the Multi-Mode model 95 and the mixed-Bohm/gyro-Bohm model for Alcator C-Mod 960229042.

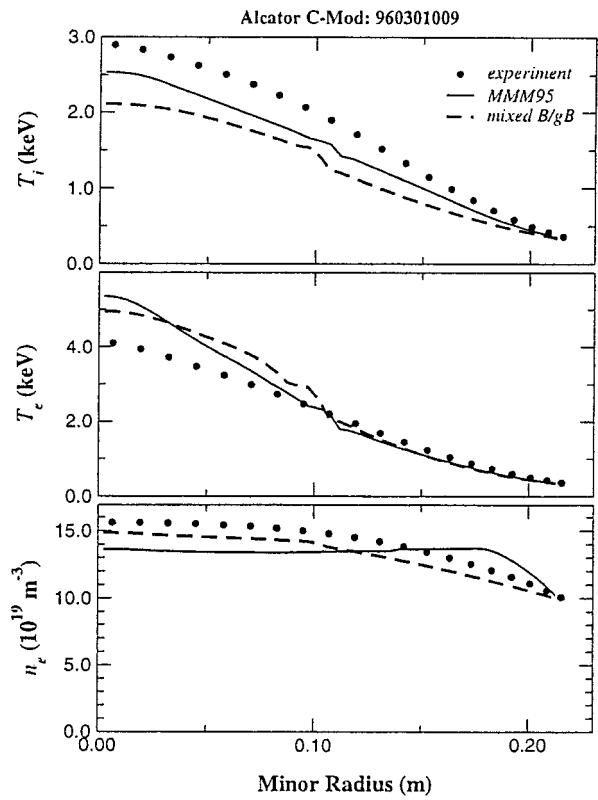


FIG. 5. Comparison of the experimental profiles ion and electron temperatures and electron density profiles with profiles predicted using the Multi-Mode model 95 and the mixed-Bohm/gyro-Bohm model for Alcator C-Mod 960301009.

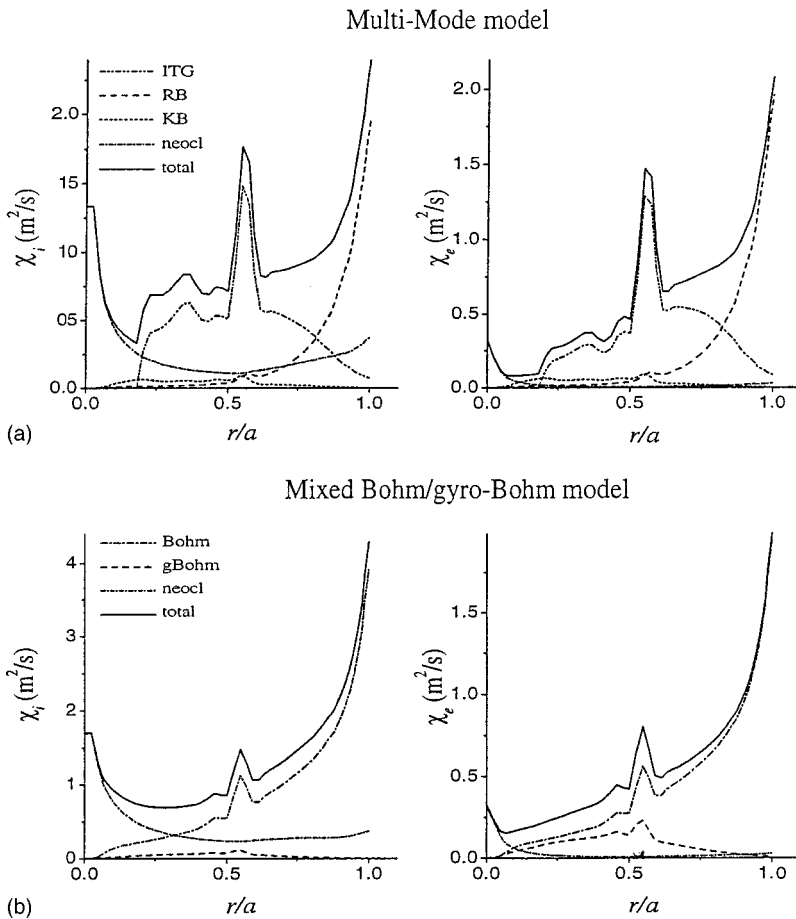


FIG. 6. Effective diffusivities from the Multi-Mode (a) and mixed-Bohm/gyro-Bohm (b) transport models for Alcator C-Mod discharge 960229042. Total diffusivities are shown by solid curves. Large dot curve represent neoclassical transport contribution. The mixed-Bohm/gyro-Bohm model has contribution from the gyro-Bohm and Bohm terms. The kinetic ballooning, resistive ballooning, and ITG/CTE modes contribute into the Multi-Mode model.

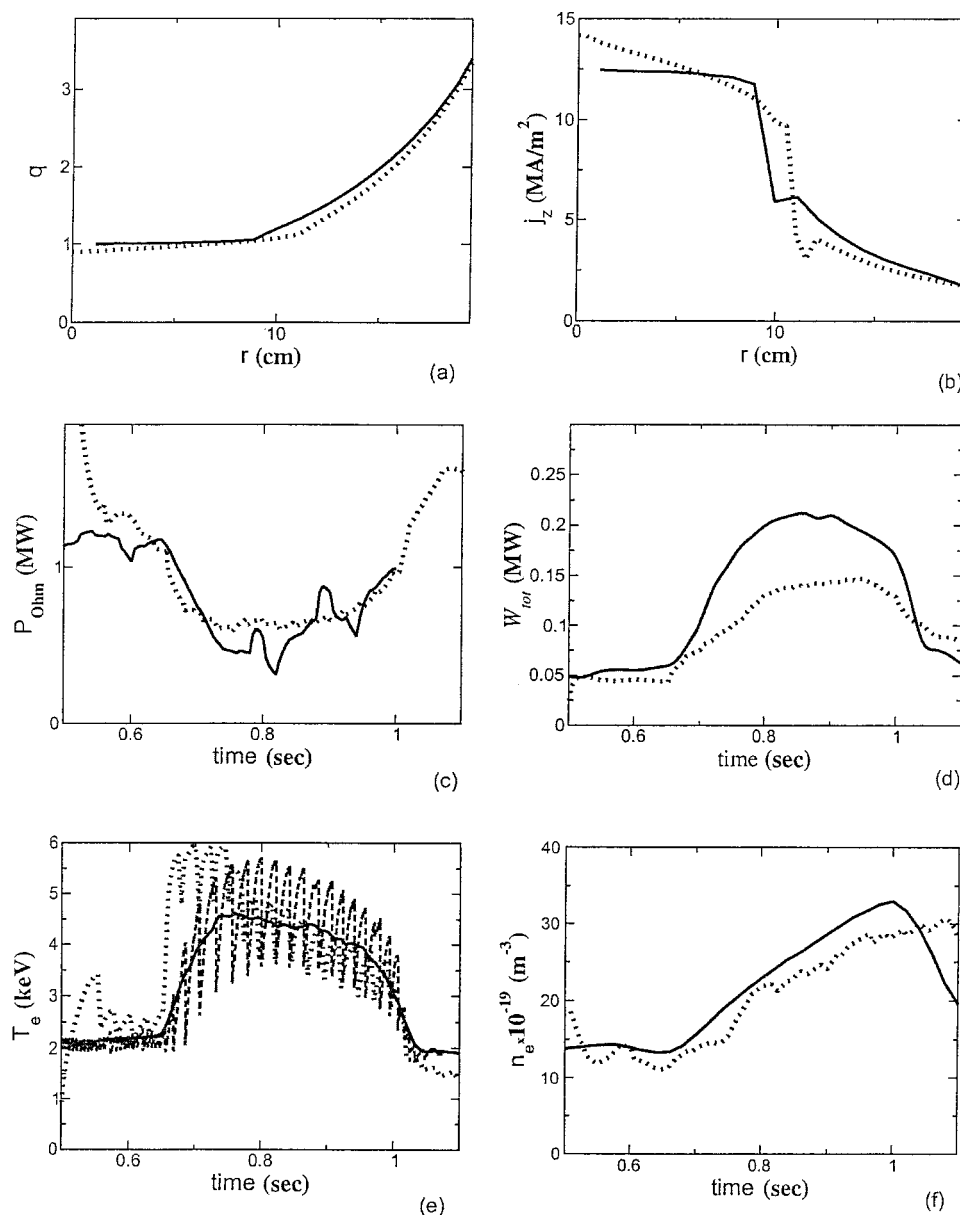


FIG. 7. Comparison of the experimental data (solid curve) for Alcator C-Mod discharge 960116024 with the simulation results, obtained with the Multi-Mode Model 95 (dotted curve): (a) q -profile vs minor radius; (b) current profile vs minor radius at 1.0 s; (c) ohmic power P_{Ohm} vs time; (d) total stored energy W_{tot} vs time; (e) electron temperature near the center $T_e^{(0)}$ vs time (TRANSP data are plotted by solid curve; ECE experimental data are curves with large dashes); (f) electron density near the center $n_e^{(0)}$ vs time.

III. In Fig. 7 the current, q -profile, time evolution of the Ohmic power, total stored energy, central electron temperature, and density for Alcator C-Mod discharge 960116024 are plotted as a function of time. Both the simulation results obtained with the BALDUR code and the data obtained from the MDSplus database are presented. Some quantities from MDSplus database are results of direct measurements, for example, the electron temperature, and the others, for example, the current, q -profile, and the total stored energy, are reconstructed using codes such as TRANSP, EFIT, SPRUCE, FPPRF, and TORIC. There is no fast ion contribution to the total energy W_{tot} in the simulations, since the ICRF heating power is read in from external data, rather than being computed internally in these BALDUR simulations. That causes the difference between the total stored energy obtained from the MDSplus database and calculated with the BALDUR code.

The profiles of the electron and ion temperature and electron density for Alcator C-Mod discharges 960116024 and 960116027 are compared with the experimental profiles

in Figs. 8 and 9. The simulations using the Multi-Mode and mixed-Bohm/gyro-Bohm models yield results that are close to one another. These results appear to be systematically slightly below the experimental data, especially for the ion temperature profiles. However, the measurements of the ion temperature have greater uncertainty than those for the electron temperature. In addition, previous BALDUR results indicate that central ion temperature is very sensitive to the boundary conditions.⁴ The uncertainties in the measurements or interpolations of ion temperature at the edge of plasma can lead to discrepancies at the center. Another factor, which affects the ion temperature profiles, is the flow shear effect. Previously published simulations of Alcator C-Mod discharges do not indicate a strong flow shear effect.⁴⁹ Toroidal velocity measurements for the seven discharges considered are not available. Estimation of the flow shear effect without toroidal velocity leads to minor alterations of the ion temperature profiles and cannot explain all differences between simulations and data. For example, when a simulation is run

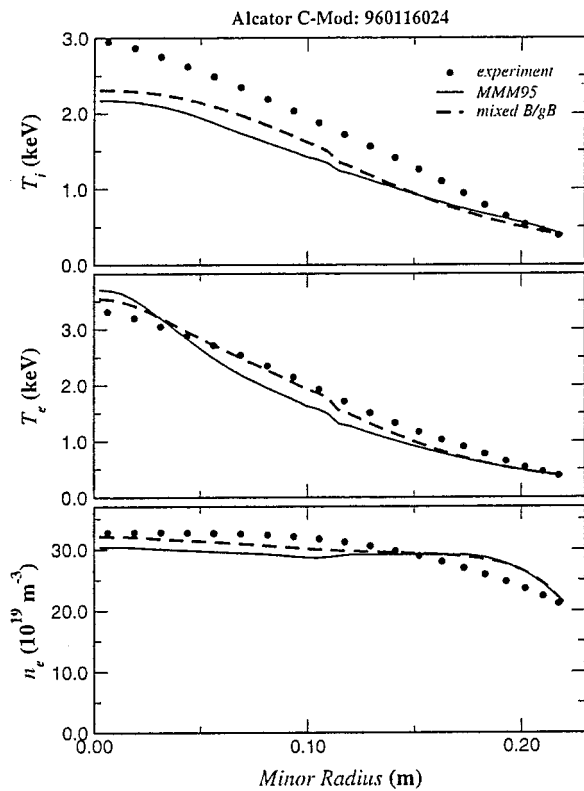


FIG. 8. Comparison of the experimental profiles ion and electron temperatures and electron density profiles with profiles predicted using the Multi-Mode model 95 and the mixed-Bohm/gyro-Bohm model for Alcator C-Mod 960116024.

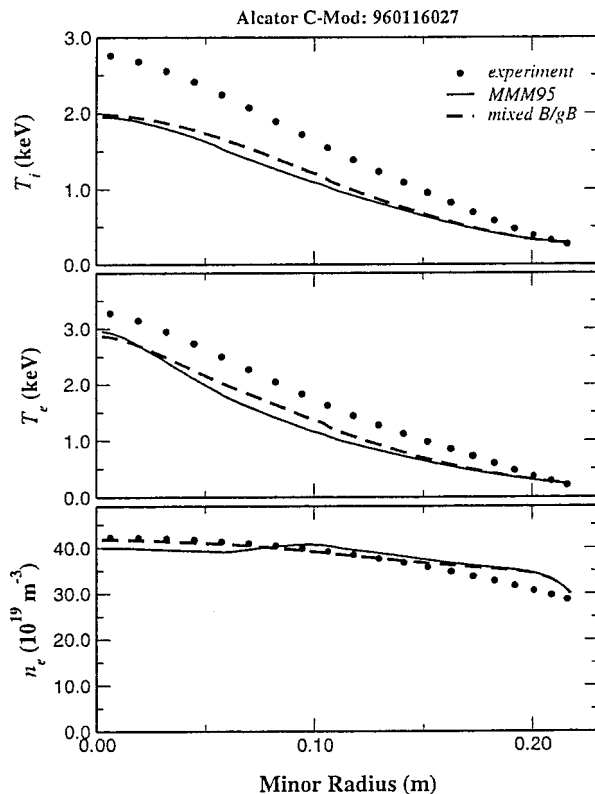


FIG. 9. Comparison of the experimental profiles ion and electron temperatures and electron density profiles with profiles predicted using the Multi-Mode model 95 and the mixed-Bohm/gyro-Bohm model for Alcator C-Mod 960116027.

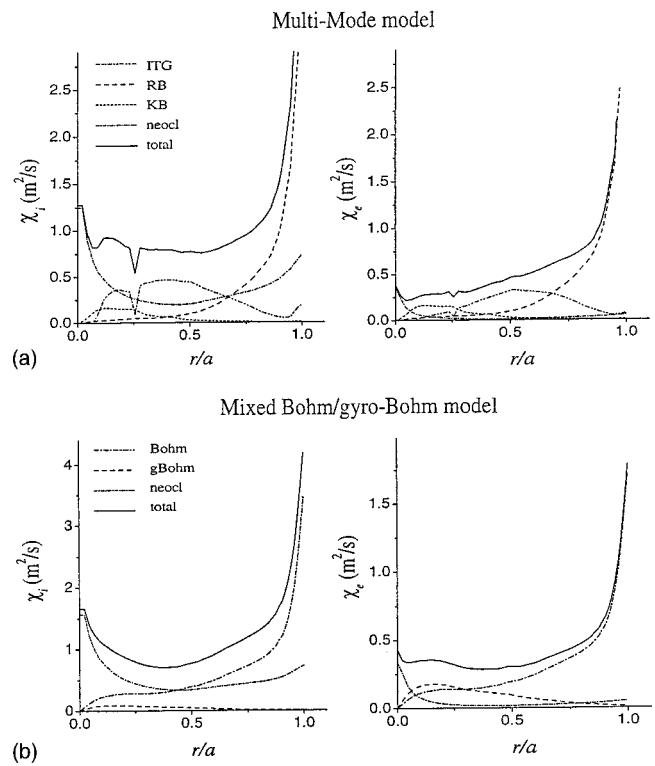


FIG. 10. Effective diffusivities from the Multi-Mode (a) and mixed-Bohm/gyro-Bohm (b) transport models for Alcator C-Mod discharge 960116027. Total diffusivities are shown by solid curves. Large dot curve represent neoclassical transport contribution. The mixed-Bohm/gyro-Bohm model has contribution from the gyro-Bohm and Bohm terms. The kinetic ballooning, resistive ballooning, and ITG/CTE modes contribute into the Multi-Mode model.

for Alcator C-Mod discharge 960116024 using only flow shear, the diamagnetic and poloidal velocity included, and using the Multi-Mode model, the normalized offset [see Eq. (5) below] is changed from -13.3% to -10.2% . The calculated electron temperature is in much better agreement with the experimental data, although the sawtooth oscillation amplitude calculated with BALDUR are smaller than observed in the experiment (see Fig. 7). Note, the central electron density computed with TRANSP does not display any sawtooth oscillations.

The effective thermal diffusivities for both transport models show behavior, which is similar to that observed for L-mode discharges (see Fig. 10). The Alcator C-Mod discharges considered in this paper have a limited range of toroidal magnetic field, 5.21 to 5.42 T. This precludes an analysis of the predicted thermal diffusivity scaling with ρ_* .

V. STATISTICAL ANALYSIS

In order to compare transport models and to estimate the sensitivity of the predictions, we compute the offset f and the rms deviation σ of the predicted electron and ion temperatures and electron density with respect to the experimental values. The technique used is described in Ref. 4. The values of f and σ are given by:

TABLE IV. Statistical results for Alcator C-Mod L-mode discharges.

| | 950407013 | | 960126007 | | 960229042 | | 960301009 | |
|---------------|-----------|--------|-----------|--------|-----------|--------|-----------|--------|
| | MMM95 | JET | MMM95 | JET | MMM95 | JET | MMM95 | JET |
| f_{ne} | -0.024 | -0.013 | -0.067 | -0.080 | -0.027 | -0.026 | -0.104 | -0.050 |
| f_{Te} | -0.051 | -0.043 | -0.065 | -0.241 | -0.030 | -0.010 | 0.046 | 0.059 |
| f_{Ti} | -0.028 | -0.036 | 0.069 | 0.268 | 0.062 | 0.074 | -0.087 | -0.154 |
| σ_{ne} | 0.018 | 0.066 | 0.081 | 0.040 | 0.035 | 0.085 | 0.090 | 0.055 |
| σ_{Te} | 0.064 | 0.060 | 0.514 | 0.307 | 0.042 | 0.044 | 0.120 | 0.125 |
| σ_{Ti} | 0.103 | 0.100 | 0.048 | 0.178 | 0.112 | 0.177 | 0.099 | 0.175 |

$$f^{(k)} \equiv \frac{1}{N} \sum_{j=1}^N \epsilon_j^{(k)} \quad (5)$$

and

$$\sigma^{(k)} \equiv \sqrt{\frac{1}{N} \sum_{j=1}^N (\epsilon_j^{(k)})^2}, \quad (6)$$

where N is the total number of experimental data points within a given discharge and k represents different discharges. These quantities are defined in terms of the deviation ϵ_j between the j th experimental data point X_j^{exp} and the corresponding simulation point X_j^{sim} :

$$\epsilon_j^{(k)} \equiv \frac{X^{(k)\text{sim}}(R_j) - X_j^{(k)\text{exp}}}{X_0^{\text{exp}(k)}}. \quad (7)$$

Note, $X_0^{\text{exp}(k)}$ is the central experimental value. This choice of normalization is discussed below.

The root-mean-square deviation σ is a measure of the scattering of the simulation profile about the experimental data. The offset f indicates whether a simulated profile is underpredicted ($f < 0$) or overpredicted ($f > 0$), compared with the experimental data. In the ideal case of a simulation profile that exactly matches the experimental data, both f and σ would be zero.

An important issue in the statistical analysis is the selection of the normalization factor. Normalizing the deviations by the local experimental values would have the effect of overweighting the rms deviation with the small values of temperature and density at the edge of the plasma. Alternatively, normalizing the deviations by the central values will yield a smaller rms deviation, but all the data points will be equally weighted. Alternatively, one could normalize with the average temperature or density. The relative comparison of rms deviation would remain the same as when the central experimental values are used. Since we are more interested in the central values of temperatures and densities, we normalize deviations [Eq. (7)] by central experimental values, $X_0^{\text{exp}(k)}$.

For the discharges, the average rms deviation, $\bar{\sigma}$, the rms deviation of f , σ_f , and the average rms deviation of σ_f , $\bar{\sigma}_f$, are given by

$$\bar{\sigma} \equiv \frac{1}{K} \sum_{k=1}^K \sigma^{(k)}, \quad (8)$$

$$\sigma_f \equiv \sqrt{\frac{1}{K-1} \sum_{k=1}^K (f^{(k)} - \bar{f})^2}, \quad (9)$$

and

$$\bar{\sigma}_f \equiv \frac{1}{K} \sum_{k=1}^K \sigma_f^{(k)}, \quad (10)$$

where K is the total number of discharges simulated.

The results of this statistical analysis are listed in Table IV for L-mode discharges and in Table V for H-mode discharges. The rms deviations are below 20% for all discharges, except Alcator C-Mod discharge 960126007, for which σ_{Te} exceeds 50%. It is concluded that this particular discharge is a real outlier. For the four L-mode and three H-mode discharges, the average rms deviation for all three profiles (T_e , T_i , and n_e) is equal to 11.3% for the Multi-Mode model and 10.5% for the mixed-Bohm/gyro-Bohm. If the Alcator C-mod outlier discharge 960126007 is excluded, then the average rms deviation for the remaining discharges is equal 9.6% for MMM95 and 9.4% and for the mixed-Bohm/gyro-Bohm transport model. In the simulations, the electron temperature appears to be underpredicted for the most of L-mode discharges and overpredicted for H-mode discharges. The ion temperature is mostly underpredicted for H-mode discharges.

The averaged rms deviation is given in Table VI separately for L-mode and H-mode discharges, and separately for the Multi-Mode and mixed-Bohm/gyro-Bohm models. Note that these tables do not include data for Alcator C-Mod discharge 960126007. Comparing the rms deviations for the electron and ion temperatures and for the electron density, one observes in Table VI that the Multi-Mode model and the

TABLE V. Statistical results for Alcator C-Mod H-mode discharges.

| | 960116024 | | 960116027 | | 960214017 | |
|---------------|-----------|--------|-----------|--------|-----------|--------|
| | MMM95 | JET | MMM95 | JET | MMM95 | JET |
| f_{ne} | -0.024 | 0.000 | 0.016 | 0.017 | -0.054 | -0.039 |
| f_{Te} | -0.048 | -0.018 | -0.118 | -0.093 | 0.052 | -0.047 |
| f_{Ti} | -0.133 | -0.106 | -0.155 | -0.135 | 0.125 | 0.043 |
| σ_{ne} | 0.074 | 0.050 | 0.052 | 0.039 | 0.110 | 0.073 |
| σ_{Te} | 0.084 | 0.044 | 0.135 | 0.104 | 0.113 | 0.147 |
| σ_{Ti} | 0.160 | 0.121 | 0.184 | 0.160 | 0.137 | 0.061 |

TABLE VI. Average rms deviations.

| | MMM95 | JET | Both models |
|--------------------------------------|-------|-------|-------------|
| $\bar{\sigma}_{n_e}^{\text{L-mode}}$ | 0.048 | 0.069 | 0.058 |
| $\bar{\sigma}_{T_e}^{\text{L-mode}}$ | 0.075 | 0.076 | 0.076 |
| $\bar{\sigma}_{T_i}^{\text{L-mode}}$ | 0.104 | 0.151 | 0.127 |
| $\bar{\sigma}_{n_e}^{\text{H-mode}}$ | 0.079 | 0.054 | 0.066 |
| $\bar{\sigma}_{T_e}^{\text{H-mode}}$ | 0.111 | 0.098 | 0.105 |
| $\bar{\sigma}_{T_i}^{\text{H-mode}}$ | 0.160 | 0.114 | 0.137 |
| $\bar{\sigma}_{n_e}$ | 0.063 | 0.061 | 0.062 |
| $\bar{\sigma}_{T_e}$ | 0.093 | 0.087 | 0.090 |
| $\bar{\sigma}_{T_i}$ | 0.132 | 0.132 | 0.132 |

mixed-Bohm/gyro-Bohm model both reproduce experimental electron temperature with almost same average rms deviation, approximately 9%. For the electron density, the rms deviations are 6.3% for the Multi-Mode model and 6.1% for the mixed-Bohm/gyro-Bohm model. The ion temperatures have larger rms deviations, 13.2% for both the Multi-Mode model and mixed-Bohm/gyro-Bohm model.

We compare $|\bar{f}^{\text{JET}} - \bar{f}^{\text{MMM}}|$ and $\bar{\sigma}_f^{\text{JET}} + \bar{\sigma}_f^{\text{MMM}}$ in Table VII, in order to estimate whether the Multi-Mode model and the mixed-Bohm/gyro-Bohm models give statistically significant different results. For all computed profiles, $|\bar{f}^{\text{JET}} - \bar{f}^{\text{MMM}}| < \bar{\sigma}_f^{\text{JET}} + \bar{\sigma}_f^{\text{MMM}}$, which implies that the two models yield statistically similar results.

VI. CONCLUSIONS

A set of Alcator C-Mod discharges with different operational scenarios and confinement modes have been simulated. These discharges are different from the discharges in other tokamaks for which simulations previously have been carried out using the BALDUR code with the Multi-Mode and mixed-Bohm/gyro-Bohm models. In particular, Alcator C-Mod operates at a much higher density range than the discharges simulated previously with the BALDUR code. As a result, the collisionality in the Alcator C-Mod simulations exceeds collisionality regularly found in JET, TFTR, and DIII-D BALDUR simulations by more than a factor of 5. It is found that the BALDUR code functions quite well in this new operational regime. Moreover, it is found that the Multi-Mode model and the mixed-Bohm/gyro-Bohm model serve to predict profiles equally well. The calculated temperature profiles fit experimental data with an average rms deviation of 11.3% for the Multi-Mode model and 11.0% for the mixed-Bohm/gyro-Bohm model. For H-mode discharges considered in this paper, the average rms deviation for ion temperature is about 13.0%.

TABLE VII. Average offsets and rms deviations of offsets.

| | \bar{f}^{MMM} | \bar{f}^{JET} | $ \bar{f}^{\text{JET}} - \bar{f}^{\text{MMM}} $ | $\bar{\sigma}_f^{\text{JET}} + \bar{\sigma}_f^{\text{MMM}}$ |
|-------|------------------------|------------------------|---|---|
| n_e | -0.036 | -0.018 | 0.018 | 0.06 |
| T_e | -0.025 | 0.025 | 0.000 | 0.11 |
| T_i | -0.036 | -0.052 | 0.016 | 0.19 |

With the mixed-Bohm/gyro-Bohm transport model, it is found that Bohm term in the mixed-Bohm/gyro-Bohm model produces the main contribution to the ion thermal diffusivity for both L-mode and H-mode discharges. For the Multi-Mode transport model, the contribution to the ion transport is due to the ITG and resistive ballooning modes in addition to neoclassical transport.

¹ITER Physics Expert Group on Confinement and Transport and Confinement Modeling and Database, ITER Physics Basis Editors, and ITER EDA, Nucl. Fusion **39**, 2175 (1999).

²J. E. Kinsey, R. E. Waltz, and D. P. Schissel, in *Proceedings, European Physical Society Meeting, Berchtesgaten, Germany, 1997* (European Physical Society, Petit-Lancy, Switzerland, 1998).

³G. Bateman, J. Weiland, H. Nordman, J. E. Kinsey, and C. Singer, Phys. Scr. **51**, 597 (1995).

⁴J. E. Kinsey and G. Bateman, Phys. Plasmas **3**, 3344 (1996).

⁵G. Bateman, A. Kritiz, J. Kinsey, and A. Redd, Phys. Plasmas **5**, 1793 (1998).

⁶M. Erba, A. Cherubini, V. Parail, E. Springmann, and A. Taroni, Plasma Phys. Controlled Fusion **39**, 261 (1997).

⁷M. Erba, T. Aniel, V. Basiuk, E. Becoulet, and X. Litaudon, Nucl. Fusion **38**, 1013 (1998).

⁸M. Erba, W. Horton, and M. Ottaviani, Nucl. Fusion **39**, 495 (1999).

⁹C. E. Singer, D. E. Post, D. R. Mikkelsen, M. H. Redi, A. McKenney, A. Silverman, F. G. P. Seidl, P. H. Rutherford, R. J. Hawryluk, W. D. Langer *et al.*, Comput. Phys. Commun. **49**, 275 (1988).

¹⁰S. C. Guo, J. Weiland, and A. Jarmen, Nucl. Fusion **37**, 1095 (1997).

¹¹P. Guzdar, J. Drake, D. McCarthy, and A. Hassam, Phys. Fluids B **5**, 3712 (1993).

¹²M. C. Zarnstorff, C. W. Barnes, P. C. E. *et al.*, in *Plasma Physics and Controlled Nuclear Fusion Research, 1990, Washington* (International Atomic Energy Agency, Vienna, 1991), Vol. 1, p. 109.

¹³G. L. Jahns, R. J. Groebner, and H. S. John, Nucl. Fusion **29**, 1271 (1989).

¹⁴P. H. Rebut, R. J. Bickerton, and B. E. Keen, Nucl. Fusion **25**, 1011 (1985).

¹⁵T. Onjun, G. Bateman, A. H. Kritiz, and D. Hannum, Phys. Plasmas **8**, 975 (2001).

¹⁶D. Hannum, G. Bateman, J. Kinsey, A. H. Kritiz, T. Onjun, and A. Pankin, Phys. Plasmas **8**, 964 (2001).

¹⁷I. Hutchinson, R. Boivin, F. Bombarda, P. Bonoli, S. Fairfax, J. G. C. Fiore, S. Golovato, R. Granetz, M. Greenwald, S. Horne *et al.*, Phys. Plasmas **1**, 1511 (1994).

¹⁸M. Greenwald, R. L. Boivin, F. Bombarda, P. Bonoli, C. L. Fiore, D. Garnier, J. A. Goetz, S. N. Golovato, M. A. Graf, R. S. Granetz *et al.*, Nucl. Fusion **37**, 793 (1997).

¹⁹M. Greenwald, R. Boivin, P. Bonoli, R. Budny, C. Fiore, J. Goetz, R. Granetz, A. Hubbard, I. Hutchinson, J. Irby *et al.*, Phys. Plasmas **6**, 1943 (1999).

²⁰D. M. Meade, Comments Plasma Phys. Controlled Fusion **2**, 81 (2000).

²¹B. Coppi, M. Nassi, and L. E. Sugiyama, Phys. Scr. **45**, 112 (1992).

²²A. Airolidi and G. Cenacchi, Nucl. Fusion **41**, 687 (2001).

²³S. P. Hirshman and J. C. Whitson, Phys. Fluids **26**, 3553 (1983).

²⁴S. P. Hirshman and D. K. Lee, Comput. Phys. Commun. **39**, 161 (1986).

²⁵B. Kadomtsev, Sov. J. Plasma Phys. **1**, 295 (1975).

²⁶G. Bateman, A. Kritiz, J. Kinsey, and A. Redd, Phys. Plasmas **5**, 2355 (1998).

²⁷P. Strand, H. Nordman, J. Weiland, and J. Christiansen, Nucl. Fusion **38**, 545 (1998).

²⁸M. Erba, V. Parail, E. Springmann, and A. Taroni, Plasma Phys. Controlled Fusion **37**, 1249 (1995).

²⁹R. J. Hawryluk, S. Suckewer, and S. P. Hirshman, Nucl. Fusion **19**, 607 (1979).

³⁰C. S. Chang and F. L. Hinton, Phys. Fluids **29**, 3314 (1986).

³¹M. Greenwald, R. Boivin, F. Bombarda, P. Bonoli, C. Christensen, C. Fiore, D. Garnier, J. Goetz, S. Golovato, M. Graf *et al.*, Phys. Plasmas **2**, 6 (1995).

³²J. A. Snipes, R. L. Boivin, C. Christensen, C. Fiore, D. Garnier, S. N. G. J. Goetz, M. Graf, R. S. Granetz, M. Greenwald, A. Hubbard *et al.*, Phys. Plasmas **3**, 1992 (1996).

³³Y. Takase, R. L. Boivin, F. Bombarda, C. C. P. T. Bonoli, C. Fiore, D.

- Garnier, J. A. Goetz, S. N. Golovato, R. Granetz, M. Greenwald *et al.*, *Phys. Plasmas* **4**, 1647 (1997).
- ³⁴Y. Takase, R. L. Boivin, F. Bombarda, P. T. Bonoli, C. L. Fiore, J. A. G. D. Garnier, S. N. Golovato, R. S. Granetz, M. J. Greenwald, S. F. Horne *et al.*, *Plasma Phys. Controlled Fusion* **38**, 2215 (1996).
- ³⁵M. Greenwald, J. Rice, R. L. Boivin, P. Bonoli, R. Budny, C. Chang, D. Ernst, C. Fiore, J. Goetz, R. Granetz *et al.*, in *Proceedings, International Atomic Energy Agency 17th Conference on Plasma Physics and Controlled Nuclear Fusion Research, Yokohama, 1998* (International Atomic Energy Agency, Austria, 1999), Vol. 1/P, p. 281.
- ³⁶B. J. D. Tubbing, B. Balet, D. V. Bartlett, C. D. Challis, R. D. G. S. Corti, C. Gormezano, C. W. Gowers, M. von Hellermann, M. Hugon, J. J. Jacquinet *et al.*, *Nucl. Fusion* **31**, 839 (1991).
- ³⁷C. L. Fiore, J. E. Rice, P. T. Bonoli, R. L. Boivin, J. A. Goetz, A. E. Hubbard, I. H. Hutchinson, R. S. Granetz, M. J. Greenwald, E. S. Marmor *et al.*, *Phys. Plasmas* **8**, 2023 (2001).
- ³⁸F. Bombarda, P. T. Bonoli, B. Coppi, R. S. Granetz, A. Hubbard, J. H. Irby, S. Migliuolo, P. O'Shea, J. E. Rice, Y. Takase *et al.*, *Nucl. Fusion* **38**, 1861 (1998).
- ³⁹Y. Lin, J. Irby, P. Stek, I. Hutchinson, J. Snipes, R. Nazikian, and M. McCarthy, *Rev. Sci. Instrum.* **70**, 1078 (1999).
- ⁴⁰A. E. Hubbard, R. L. Boivin, R. S. Granetz, M. Greenwald, I. H. Hutchinson, J. H. Irby, J. In, B. Kesner, B. Labombard, Y. Lin *et al.*, *Phys. Plasmas* **5**, 1744 (1998).
- ⁴¹P. J. O'Shea, Ph.D. thesis, MIT, Cambridge, MA (1997).
- ⁴²D. A. Mossessian, A. Hubbard, and J. Irby, *Rev. Sci. Instrum.* **70**, 759 (1999).
- ⁴³R. L. Boivin, J. A. Goetz, E. S. Marmor, J. E. Rice, and J. L. Terry, *Rev. Sci. Instrum.* **70**, 260 (1999).
- ⁴⁴G. Hammett, Ph.D. thesis, Princeton University, Princeton, NJ (1986).
- ⁴⁵M. Brambilla and T. Krucke, *Nucl. Fusion* **28**, 1813 (1988).
- ⁴⁶L. L. Lao, H. S. John, R. D. Stambaugh, A. G. Kellman, and W. Pfeiffer, *Nucl. Fusion* **25**, 1611 (1985).
- ⁴⁷R. J. Goldston, D. C. McCune, H. H. Towner, S. L. Davis, R. J. Hawryluc, and G. L. Schmidt, *J. Comput. Phys.* **43**, 61 (1981).
- ⁴⁸D. N. Smithe, P. L. Colestock, R. J. Kashuba, and T. Kammash, *Nucl. Fusion* **27**, 1319 (1987).
- ⁴⁹J. Schachter, Ph.D. thesis, MIT, Cambridge, MA (1997).